

Article

Effect of Metal-Oxide Phase on the Magnetic and Magnetocaloric Properties of $\text{La}_{0.7}\text{Ca}_{0.3}\text{MnO}_3$ -MO (MO=CuO, CoO, and NiO) Composite

Surendra Dhungana¹, Jacob Casey², Dipesh Neupane¹, Arjun K. Pathak² , Sunil Karna^{3,*} 
and Sanjay R. Mishra^{1,*}

¹ Department of Physics and Materials Science, The University of Memphis, Memphis, TN 38152, USA

² Department of Physics, SUNY Buffalo State, Buffalo, NY 14222, USA

³ Department of Natural Science, Union College, Barbourville, KY 40906, USA

* Correspondence: skarna@unionky.edu (S.K.); srmishra@memphis.edu (S.R.M.)

Abstract: The study reports the synthesis and characterization of the magnetic and magnetocaloric effects of metal-oxide (MO) modified $\text{La}_{0.7}\text{Ca}_{0.3}\text{MnO}_3$ perovskites manganite. The powder composite samples, with a nominal composition of $(1-x)\text{La}_{0.7}\text{Ca}_{0.3}\text{MnO}_3-x\text{MO}$ (Wt.% $x = 0.0, 2.5, 5.0$), were prepared using the facile autocombustion method, followed by an annealing process. The phase purity and structure were confirmed by X-ray diffraction. Temperature and field-dependent magnetization measurements and Arrott analysis revealed mixed first- and second-order phase transition (ferromagnetic to paramagnetic) in composite samples. The phase transition temperature shifted to lower temperatures with the addition of MO in the composite. A large magnetic entropy change ($4.75 \text{ J Kg}^{-1}\text{K}^{-1}$ at 1T and $8.77 \text{ J Kg}^{-1}\text{K}^{-1}$ at 5T) was observed in the $\text{La}_{0.7}\text{Ca}_{0.3}\text{MnO}_3$ (LCMO) sample and was suppressed, due to the presence of the MO phase in the composite samples. On the other hand, the addition of MO as a secondary phase in the LCMO samples enhanced their relative cooling power (RCP). The RCP of all composite samples increased with respect to the pristine LCMO, except for LCMO-5%NiO. The highest RCP value of 267 J Kg^{-1} was observed in LCMO-5%CuO samples, which was 23.4% higher than the 213 J Kg^{-1} observed for the pure LCMO at a magnetic field of 5T. The enhanced RCP of these composites makes them attractive for potential refrigeration applications.

Keywords: autocombustion; magnetocaloric; perovskite; LCMO; refrigerant; composite



Citation: Dhungana, S.; Casey, J.; Neupane, D.; Pathak, A.K.; Karna, S.; Mishra, S.R. Effect of Metal-Oxide Phase on the Magnetic and Magnetocaloric Properties of $\text{La}_{0.7}\text{Ca}_{0.3}\text{MnO}_3$ -MO (MO=CuO, CoO, and NiO) Composite. *Magnetochemistry* **2022**, *8*, 163. <https://doi.org/10.3390/magnetochemistry8120163>

Academic Editor: Hui Shen

Received: 20 October 2022

Accepted: 18 November 2022

Published: 22 November 2022

Publisher's Note: MDPI stays neutral with regard to jurisdictional claims in published maps and institutional affiliations.



Copyright: © 2022 by the authors. Licensee MDPI, Basel, Switzerland. This article is an open access article distributed under the terms and conditions of the Creative Commons Attribution (CC BY) license (<https://creativecommons.org/licenses/by/4.0/>).

1. Introduction

The scientific community is actively engaged in materializing energy-efficient and environmentally friendly technologies to mitigate increasing energy demands. Low power refrigeration or cooling has emerged as a potential alternative for future energy-saving [1–4]. Common cooling techniques include absorption/adsorption refrigerators, ejector refrigeration systems and, less commonly, thermoelectric cooling, thermoacoustic refrigerators, and magnetocaloric (MC) refrigeration [5]. Magnetocaloric effect (MCE) units have excellent prospects for cooling technology, due to their cooling efficiency, environmental friendliness, reliability, portability, cost-effectiveness, and long cyclic operational stability.

The magnetocaloric effect (MCE) is a magneto-thermodynamic phenomenon in which the thermal state of magnetic materials changes in response to an applied magnetic field [6,7]. At the heart of MCE lies the coupling between the magnetic moments and external magnetic field, and, in some cases, the MCE involves structural transitions concomitant with magnetic transitions [8]. The magnetocaloric material (MCM) should have a high magnetic entropy change, a wide range of operating temperatures, low hysteresis loss, low specific heat, high thermal conductivity, etc., to produce a large MCE response, which is challenging to meet. Recent advances promise improved MCE efficiency and address challenges like fabrication complexity, less resistance to corrosion, poor conductivity, etc. [9].

Different metallic alloys (e.g., iron-based alloy $\text{Gd}_5\text{Ge}_{1.9}\text{Si}_2\text{Fe}_{0.1}$) [10] and composites e.g., $\text{La}(\text{Fe},\text{Si})_{13}/\text{CuLa}(\text{Fe},\text{Si})_{13}\text{H}_y/\text{In}$, Refs. [1,11] showed potential to overcome deficiencies, henceforth, improving the performance of MCE-based magnetic refrigeration or cooling.

However, these metallic materials are expensive, difficult to synthesize, and easily corrode, limiting their use in various applications. Recently, strontium-doped lanthanum manganite, with the general formula $\text{La}_{1-x}\text{Sr}_x\text{MnO}_3$, $x = 0.0 < 1.0$ (LSMO), has attracted much attention for its potential magnetocaloric materials at near room temperature [12–16]. Current literature is replete with studies on $\text{RE}_{1-x}\text{M}_x\text{MnO}_3$ type MCM. The search for oxide-based MCM ensued because they are corrosion-resistant, stress-resistant, easy to synthesize, have long cyclic stability and their magnetic properties can easily be tuned. Recently, it was reported that in multiphase composite materials, the temperature dependence of entropy change, $-\Delta S_M$, curve broadens with enhanced relative cooling power (RCP) values [17–19]. According to theoretical studies, $-\Delta S_M$ and RCP of the composites are predicted to show promising results [20–22].

Large RCP values can be achieved by MCM composite with suitable transition temperatures as it undergoes multiple magnetic phase transitions [22,23]. El Boukili et al. reported that the transition temperature remained unchanged but decrease in ΔS_{max} and increase in RCP were recorded on increasing the content of Mn_2O_3 in $(1-x)\text{La}_{0.6}\text{Ca}_{0.4}\text{MnO}_3/x\text{Mn}_2\text{O}_3$ composite synthesized via solid-state reaction [24]. The drop in transition temperature and ΔS_{max} values, along with the increase in RCP value by introducing Co_3O_4 in $\text{La}_{0.7}\text{Sr}_{0.3}\text{MnO}_3/\text{Co}_3\text{O}_4$ and $\text{La}_{0.7}\text{Ca}_{0.3}\text{MnO}_3/\text{Co}_3\text{O}_4$ composites synthesized via solid state reaction, was reported by Anwar et al. The antiferromagnetic (AFM) nature of Co_3O_4 induces magnetic inhomogeneity in the ferromagnetic perovskite to make these changes [25]. Nasi et al. synthesized $\text{La}_{0.6}\text{Sr}_{0.4}\text{MnO}_3/x(\text{Sb}_2\text{O}_3)$ composites using a solid-state reaction and found that the ΔS_{max} and RCP values dropped, compared to pure perovskite, due to the decrease in delocalization of the electron that minimizes the double-exchange interaction. However, the transition temperature remained constant, implying that the Sb_2O_3 phase remained only at the grain boundaries and did not react with $\text{La}_{0.6}\text{Sr}_{0.4}\text{MnO}_3$ to be included within the perovskite structure [26]. Gavrilova et al. synthesized $(1-x)\text{La}_{0.7}\text{Sr}_{0.3}\text{MnO}_3/x\text{NaF}$ composites using a solid-state reaction and found that the magnetic entropy and transition temperature dropped due to the introduction of the secondary NaF phase, which was the contribution of grain size reduction. However, the RCP values did not change significantly, due to magnetic inhomogeneity [27]. Neupane et al. reported that the values of ΔS_{max} increased, while the value of RCP decreased, with increasing metal oxides in $\text{La}_{0.45}\text{Nd}_{0.25}\text{Sr}_{0.3}\text{MnO}_3/\text{MO}$ ($\text{MO}=\text{CuO}$, CoO , and NiO) composites synthesized via the autocombustion method. The proximity of the perovskite's phase transition temperature and those of the metal oxides and the size of grains influenced the values of ΔS_{max} and RCP [28]. An exchange bias interfacial FM/AFM effect was reported in $(\text{LaFeO}_3)_x-(\text{La}_{0.7}\text{Ca}_{0.3}\text{MnO}_3)_{1-x}$ composite thin films prepared via pulsed laser deposition [29]. At the same time, the impact of NiO particles was investigated on the magnetoresistance properties of LACM-NiO composites and it was realized that the NiO nanoparticles limited the charge transport in the composites to increase resistivity [30]. Thus, understanding the role of the secondary oxide phase in the manganite composite is essential in designing high-performance magnetocaloric and spintronic materials, and for their applications [31,32].

The literature shows that composite formation causes decrease in ΔS_{max} but increase in the RCP by increasing the full-width-at-half-maximum (FWHM) temperature range of ΔS vs. T curve, enhancing the operating temperature range for the magnetocaloric effect. Furthermore, the composite formation can help tune the paramagnetic (PM)-ferromagnetic (FM) transition temperature. Moreover, the literature abundantly shows the use of solid-state reactions to synthesize manganite and composites. The autocombustion route for synthesizing manganites and composites has not, however, been widely reported. The sol-gel autocombustion method is based on the contribution of both sol-gel and combustion processes [33]. The autocombustion process involves self-sustained redox exothermic reactions between hydrated metal nitrates and fuel(s) mixed on the molecular level [34–36].

The main advantages of autocombustion are fast and straightforward processing (the formation results in an oxide mixture within a few seconds), with relatively low-cost precursors (usually nitrate salts), no need for special equipment, low energy consumption, atomic-level diffusion, and a resulting powder that is ultrafine and homogeneous [37–39].

In the present study, a single calcium-doped Lanthanum manganate $\text{La}_{0.7}\text{Ca}_{0.3}\text{MnO}_3$ (LCMO), with the composition chosen as the perovskite phase. $\text{La}_{0.7}\text{Ca}_{0.3}\text{MnO}_3$ is reported to have high ΔS_{max} , and a paramagnetic (PM)-ferromagnetic (FM) transition temperature around room temperature [40]. We chose three antiferromagnetic (AFM) metal oxides, Mo, having Neel temperature range of 230 to 525 K ($\text{CoO}:T_N \sim 291$ K, $\text{NiO}:T_N \sim 525$ K, $\text{CuO}:T_N \sim 230$ K) [41,42]. The magnetic inhomogeneity introduced by AFM phases was observed to be beneficial in tuning the phase transition temperature and RCP value of the composite [28,43]. The present work reports enhanced RCP value for LCMO-NiO/CoO/CuO composites.

2. Experimental

Synthesis

The $(1 - x)\text{La}_{0.7}\text{Ca}_{0.3}\text{MnO}_3 - x\text{MO}$ (Wt.%, $x = 0.0\%$, 2.5% , 5.0% ; $M = \text{Ni}, \text{Cu}, \text{Co}$) composites were synthesized via the autocombustion method. The reagents grade $\text{La}(\text{NO}_3)_3 \cdot 6\text{H}_2\text{O}$, $\text{Ca}(\text{NO}_3)_2 \cdot 4\text{H}_2\text{O}$, and $\text{Mn}(\text{NO}_3)_2 \cdot 4\text{H}_2\text{O}$ precursors were used for the preparation of $\text{La}_{0.7}\text{Ca}_{0.3}\text{MnO}_3$ perovskite with Citric Acid as the fuel. Similarly, $\text{Ni}(\text{NO}_3)_2 \cdot 6\text{H}_2\text{O}$, $\text{Cu}(\text{NO}_3)_2 \cdot 3\text{H}_2\text{O}$, and $\text{Co}(\text{NO}_3)_2 \cdot 6\text{H}_2\text{O}$ were used as precursors for respective metal oxide formation with Citric Acid as fuel. All used chemicals were obtained from Sigma Aldrich (Burlington, MA, USA) with >99% purity. The synthesis process is demonstrated in the schematic given in Figure 1.

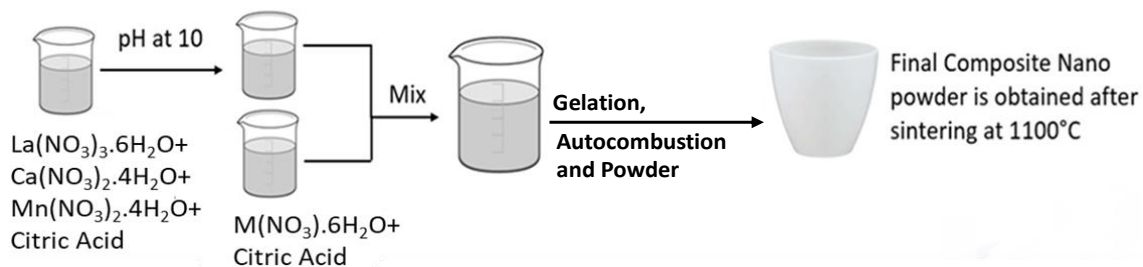
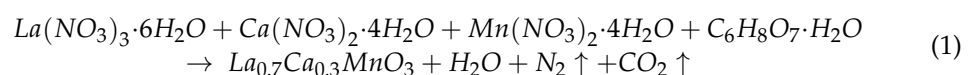


Figure 1. Schematic of preparation of LCMO-MO composite powder.

The stoichiometric amounts of $\text{La}(\text{NO}_3)_3 \cdot 6\text{H}_2\text{O}$, $\text{Ca}(\text{NO}_3)_2 \cdot 4\text{H}_2\text{O}$, $\text{Mn}(\text{NO}_3)_2 \cdot 4\text{H}_2\text{O}$, and citric acid, given in Table 1, were dissolved in 40 mL de-ionized (DI) water and ultrasonicated for one hour to form a homogeneous solution. The pH of this solution was maintained at 10 to ensure the desired nanosized synthesis of the perovskite. These two solutions were mixed, ultrasonicated for one hour, and then heated on a hot plate at 80°C for gelation. After a gel-like substance was observed, the temperature was increased to 300°C for the autocombustion. After the gel-like substance hardened into a fluffy solid phase, the product was ground to a fine powder. To obtain the desired composites, the grounded particles were finally calcined at 1100°C . The chemical reaction occurred as follows:



where,

$$M = \text{Ni}, \text{Cu}, \text{Co}.$$

Table 1. Stoichiometry of chemicals used to synthesize LCMO–MO composites.

Sample	Mass (grams)						
	La(NO ₃) ₃ ·6H ₂ O	Ca(NO ₃) ₂ ·4H ₂ O	Mn(NO ₃) ₂ ·4H ₂ O	Ni(NO ₃) ₂ ·6H ₂ O	Cu(NO ₃) ₂ ·3H ₂ O	Co(NO ₃) ₂ ·6H ₂ O	Citric Acid
LCMO	1.4284	0.3338	1.1829	-	-	-	2.9709
LCMO-2.5%NiO	1.3927	0.3255	1.1533	0.0973	-	-	2.9670
LCMO-5.0%NiO	1.3570	0.3171	1.1237	0.1946	-	-	2.9630
LCMO-2.5%CuO	1.3927	0.3255	1.1533	-	0.0731	-	2.9627
LCMO-5.0%CuO	1.3570	0.3171	1.1237	-	0.1462	-	2.9544
LCMO-2.5%CoO	1.3927	0.3255	1.1533	-	-	0.0970	2.9668
LCMO-5.0%CoO	1.3570	0.3171	1.1237	-	-	0.1941	2.9626

3. Characterization

An X-ray powder diffraction (XRD) experiment was carried out with CuK α (λ ~1.5406 Å) radiation using a Bruker (D8 Advance) diffractometer. The powder X-ray diffraction data were collected in the 2θ range from 20° to 75° with a step size of 0.042° and collection time of 0.2 s/step using a Vantec solid-state detector Bruker, Billerica, MA, USA). The magnetic properties of samples, viz. hysteresis and field-cooled (FC) and zero-field-cooled (ZFC) magnetization, were investigated, using a physical property measurement system (PPMS, Quantum Design, San Diego, CA, USA) as a function of temperature in the 5–300 K range and with a field up to 5T. The FC measurement was performed by cooling the sample down to 5 K at a 100 Oe magnetic field, followed by FC magnetization measurement as a function of temperature from 5 to 300 K. To calculate entropy change, isothermal magnetization curves were collected in a field up to 5T.

4. Results and Discussion

The room temperature XRD scans for LCMO–MO composites with different compositions are shown in Figure 2. The observed peaks of only LCMO and MO indicated the absence of any impurity formed in the composite. Since the metal oxide was only present in a small amount, as compared to the perovskite LCMO, the perovskite peak dominated the XRD spectrum, as shown in Figure 2a,c,e. In Figure 2b,d,f, long scans were performed to detect MO phases in the composites. MO peaks showed an increase in intensity with an increase in their Wt.% content in the composite samples. The XRD spectrum was refined using TOPAS Bruker, Billerica, MA, USA) software to determine the lattice parameters and cell volume of the LCMO–MO composites. given in Table 2. The X-ray diffraction analysis also showed that the LCMO perovskite existed in the orthorhombic phase (space group: Pnma, ICDD #: 00-063-0088). The metal oxides NiO (ICDD #: 01-085-5454) and CoO (ICDD #: 01-071-1178) existed in a cubic phase (space group: $Fm\bar{3}m$), whereas CuO (ICDD #: 01-086-8837) existed in the monoclinic phase (space group: C12/c1). The minimal change in the lattice volume of LCMO with MO addition in the composite was noted. However, the possibility of M ion inclusion in the perovskite structure could not be ignored.

Table 2. Lattice parameters, cell volume, unit cell anisotropy, and crystallite size of LCMO and MO phase in LCMO–MO composite samples.

Sample	La _{0.7} Ca _{0.3} MnO ₃ Phase				Metal Oxide Phase					
	a(Å) (±0.01)	b(Å) (±0.01)	c(Å) (±0.01)	δ	Cell Volume (Å ³) (±0.1)	a(Å) (±0.01)	b(Å) (±0.01)	c(Å) (±0.01)	Cell Volume (Å ³) (±0.1)	Crystallite Size (nm)
LCMO	5.46	7.71	5.47	−0.0027	230.27		NA		NA	48.85 (±4.41)
LCMO-2.5%NiO	5.46	7.71	5.46	−0.0014	229.85	3.79	NA	NA	54.42	48.01 (±4.59)
LCMO-5%NiO	5.46	7.70	5.45	−0.0015	229.13	4.29	NA	NA	79.10	42.37 (±3.92)
LCMO-2.5%CuO	5.46	7.69	5.44	−0.0025	228.41	4.69	3.32	5.13	79.88	47.70 (±4.39)
LCMO-5%CuO	5.47	7.70	5.46	−0.0028	229.97	4.78	3.37	5.16	83.12	47.15 (±4.66)
LCMO-2.5%CoO	5.41	7.68	5.44	0.00130	226.03	4.32	NA	NA	80.57	46.83 (±4.19)
LCMO-5%CoO	5.45	7.71	5.44	0.00132	228.59	4.31	NA	NA	80.25	43.06 (±3.93)

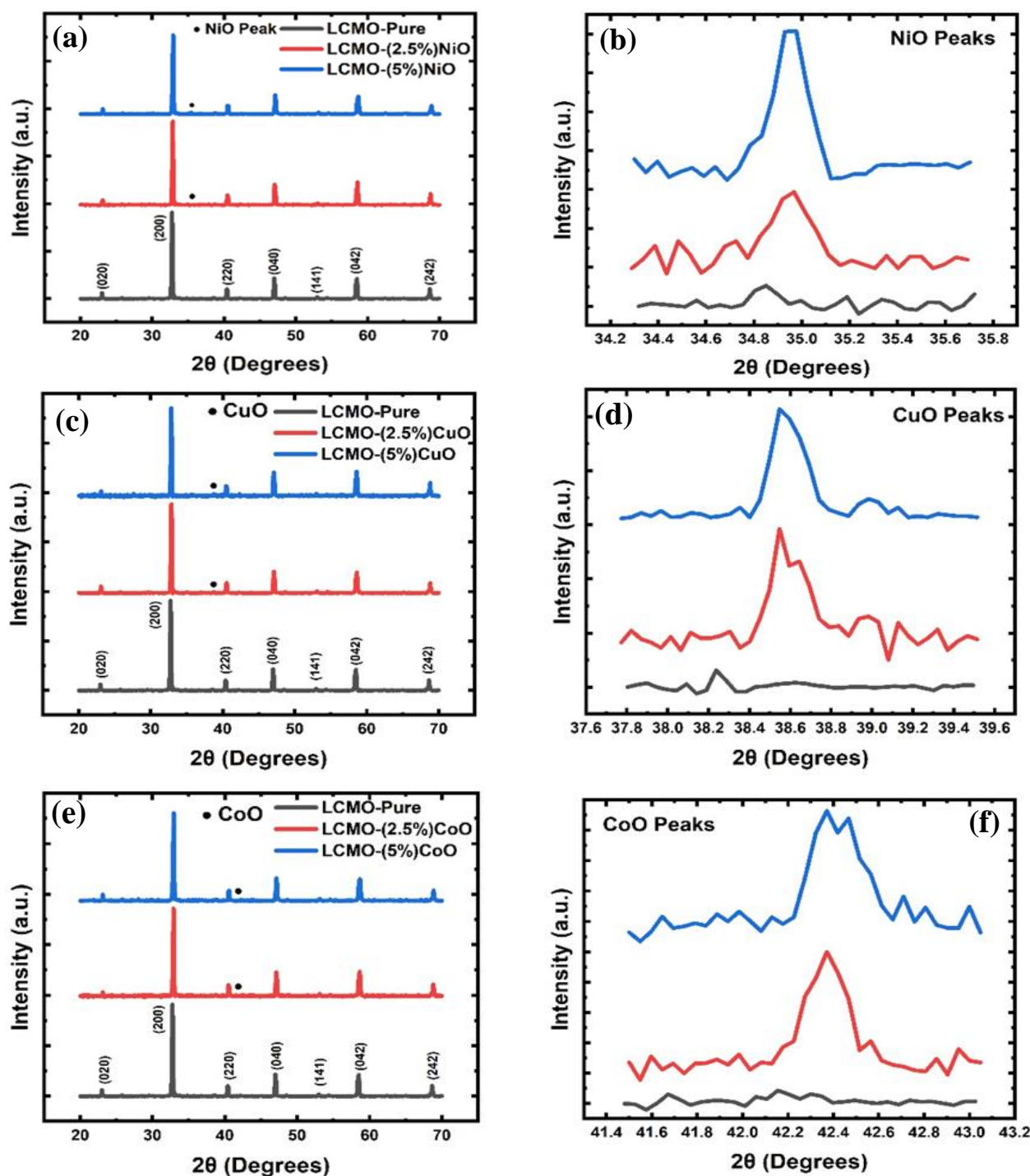


Figure 2. XRD scans of $\text{La}_{0.7}\text{Ca}_{0.3}\text{MnO}_{3-x}\% \text{MO}$ composites (a,c,e) and long scans for MO peaks (b,d,f).

Further, the crystallite size of the LCMO phase was calculated using Scherrer's method [44]. The diffraction peaks with Miller indices (hkl) values (020), (200), (220), (040), (042), and (242), corresponding to peak positions (2θ) 23.1° , 32.8° , 40.4° , 47.1° , 58.5° , and 68.7° , were used to calculate the crystallite size of the LCMO phase. The obtained crystallite size for the LCMO phase is also presented in Table 2. The LCMO lattice parameters and cell volume were similar to those reported by Shankar et al. [45]. The crystallite size of LCMO decreased as the amount of metal oxides increased. The observed grain refinement of the LCMO phase in the composite might result from the following: (a) the increased micro-strain due to the size difference between LCMO and MO [46,47]; (b) MO diffusion to

the boundaries, which could restrain the grain growth [48]; (c) the reduction in the unit cell volume accompanied by shortening the diffusion path between nearby grains, which could, consequently, result in smaller grains during calcination. Similar grain refinement was observed in other ferrites and composites [48,49]. To check for unit cell distortion, the unit cell anisotropy, δ , defined as $[(b/(a^2+c^2)^{0.5}) - 1]$, was calculated [45]. The δ parameter is listed in Table 2. The δ was zero for cubic cells. Thus, variation in δ parameter showed some evidence of deviation from the LCMO unit cell, which could result from the crystallite size reduction for these composites and/or M ion diffusion in the LCMO phase, which remained undetected in XRD. The irregular change in a lattice pattern with MO phase in Table 2 could be due to different amounts of diffusion of metal ions in the main phase. This diffusion was dependent on reaction kinetics. Some metal ions dissociated more from MO than others, thus, causing the observed difference in lattice parameters.

5. Magnetic and Magnetocaloric Study

The temperature dependence of magnetization of the composites measured in a field-cooled (FC) process during warming-up in a constant external applied field of 1 kOe is shown in Figure 3. The samples with low MO content (<5%) showed a sharp magnetic phase transition from a low-temperature ferromagnetic to a high-temperature paramagnetic phase at Curie temperature (T_C). It was noticed that the value of T_C decreased with an increasing amount of metal oxide in the composite. The curve became broader and appeared to show a second-order phase transition. The Curie temperature T_C was deduced from the minimum of dM/dT vs. T curves, as shown in insets of Figure 3. The peak of this curve represented the phase transition temperature, and the broadness of the peak suggested whether the transition was immediate or occurred over a wide range of temperatures. The obtained T_C values are listed in Table 3. The transition temperature of 258 K for pure LCMO was in close agreement with the 267 K recorded in the literature [50,51]. The transition temperature dropped on all composites with increasing content of metal oxides. The drop in transition temperature was very similar for LCMO–NiO and LCMO–CuO samples, but there was a somewhat higher drop observed for LCMO–CoO samples. A significant drop in temperature from 258 K for pristine LCMO to 167 K was observed in the LCMO–5%CoO sample. The peaks also broadened as the content of metal oxide increased. This drop-in phase transition temperature was due to the weakening of the double exchange magnetic, Mn–O–Mn interaction, possibly due to the diffusion of M ions into the LCMO matrix. The $3d$ ions brought in an unexpected variation of Mn valence states and oxygen vacancies [25,52,53]. Further, the intensity of the rate of change of magnetization, with respect to temperature, decreased with an increase in metal oxide content; thus, the temperature range of the PM–FM transition became broader in the case of composite samples, which indicated the influence of increased magnetic inhomogeneity in the sample. Thus, in composites, the phase transition ranged over a more extensive temperature range than the pristine LCMO.

Table 3. The magnetic phase transition temperature of LCMO–MO composite samples.

Sample	Phase Transition Temperature (T_C)
LCMO	258.0 K
LCMO-2.5%NiO	195.0 K
LCMO-5%NiO	173.0 K
LCMO-2.5%CuO	172.0 K
LCMO-5%CuO	194.0 K
LCMO-2.5%CoO	185.0 K
LCMO-5%CoO	167.0 K

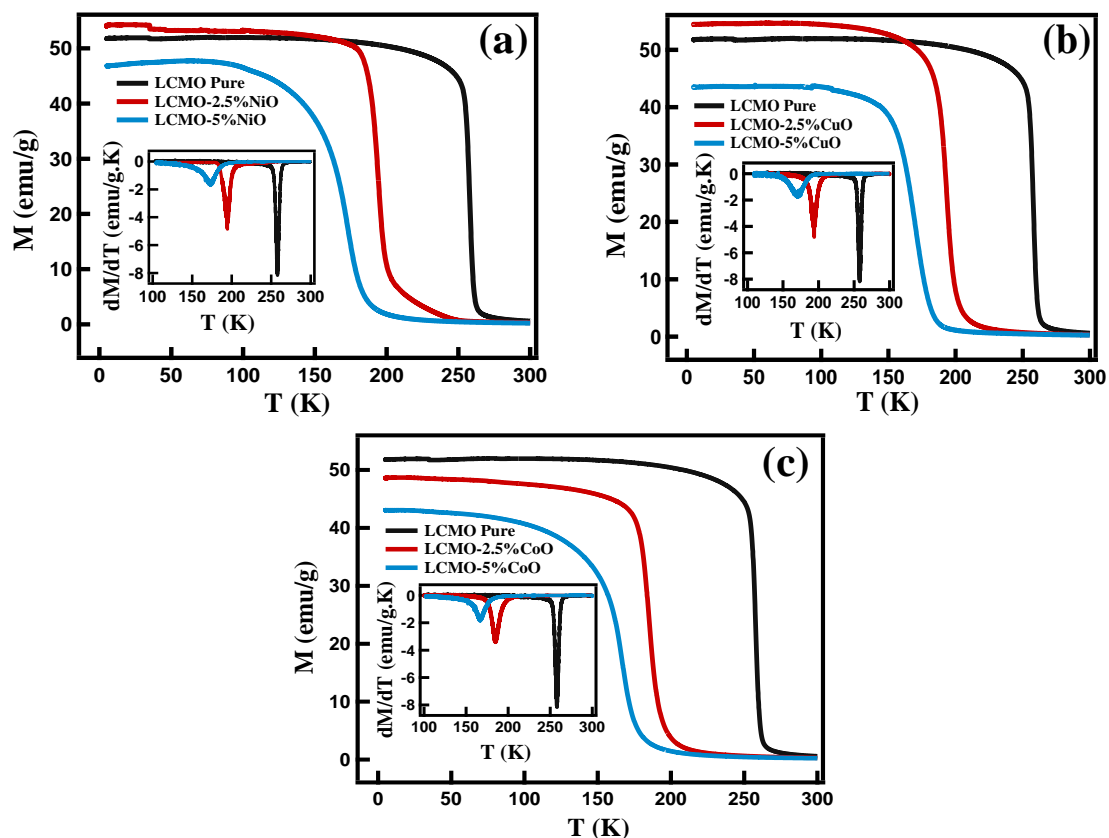


Figure 3. Field Cooled (FC) curve of LCMO-MO composite samples measured in an externally applied field of 1kOe (a) LCMO- $x\%$ NiO, (b) LCMO- $x\%$ CuO, and (c) LCMO- $x\%$ CoO. Insets show dM/dT vs. T plot.

The value of magnetization at low temperature, 5 K, was observed to decrease with the increase in MO content for LCMO–NiO and LCMO–CoO, while LCMO–CuO showed an increase at 2.5% CuO content. The magnetic interaction in LCMO was mainly governed by $Mn^{3+}-O^{2-}-Mn^{4+}$ interactions and the diffusion of Cu^{2+} into LCMO matrix substitutes for Mn^{3+} and induced more Mn^{4+} which made the $Mn^{3+}-O^{2-}-Mn^{4+}$ ferromagnetic chain increase, and, therefore, magnetization was enhanced [52]. On the other hand, superfluous Cu^{2+} resulting from an increase in CuO content in the composite occupied B sites between Mn^{3+} and Mn^{4+} , and would induce disorder and change the bond angle and bond length of Mn–O–Mn interaction, and, thus, weaken the double-exchange interaction. Accordingly, T_C and M_s decreased with the gradual increase in doping level [54,55]. A similar mechanism could be responsible for the observed decrease in magnetization at 5 K in the LCMO–MO composite. Figure 4 shows the magnetic hysteresis of LCMO–MO composites at 5 K. The $M-H$ curves indicated that the magnetization of the samples increased rapidly at low fields and then tended to saturate at high fields, reflecting the ferromagnetic behavior of LCMO–MO composites. The inset in Figure 4b shows the composites' saturation magnetization (M_s) with their weight percentage of the MO phase. The decrease in the magnetization of the composite with increased Wt.% of the MO phase could be the combined effect of the following: (1) increased Wt.% of antiferromagnetic phase; (2) decrease in particle size, as reported by He et al. [56]; (3) diffusion of metal ions into LCMO grains and grain boundaries, as explained above.

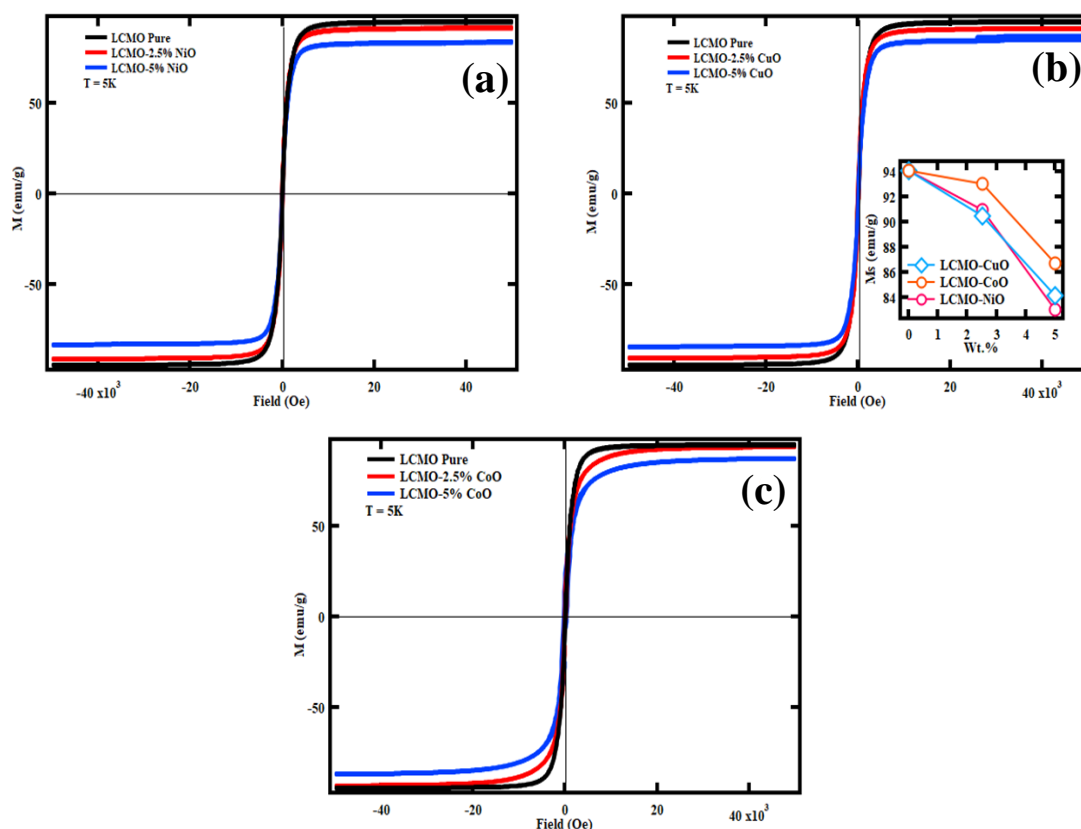


Figure 4. Magnetic hysteresis loop (M vs. H) of LCMO- $x\%$ NiO, (b) LCMO- $x\%$ CuO, and (c) LCMO- $x\%$ CoO at 5 K. The inset in figure (b) is showing the saturation of magnetization with weight percentage.

To evaluate the effect of MO content on the magnetic entropy change in LCMO-MO composite, magnetic isotherm curves were collected. Magnetic isothermal curves were collected by measuring the sample's magnetization with varying external magnetic fields at various temperatures around the phase transition temperature. The measurements were taken at an interval of 5 K to obtain more accurate data. Figure 5 represents the M vs. H plot at different temperature values for all the samples. From Figure 5, it is evident that the samples underwent a phase transition from PM-FM state with lowering temperatures. As expected, the $M-H$ curves revealed a strong variation of magnetization around the T_C . The lower portion of the graph represented the higher temperature measurements which increased gradually with the field. At lower temperatures, the graph changed nature and acquired more of a ferromagnetic ordering with the magnetization saturation in the presence of the external magnetic field. A jump in magnetization values for the same external field with a temperature decrease was noticed. The highest jump of magnetization corresponded to the phase transition temperature. This was because magnetization showed a sharp increase at the transition from the paramagnetic to the ferromagnetic phases. This indicated that a small variation in magnetic field value could significantly increase the sample's spin-ordering and magnetization.

Figure 6 represents the Arrott plots for all the samples. The negative slope corresponds to the first-order phase transition, whereas the positive slope corresponds to the second-order phase transition [57]. We observed a first-order phase transition in LCMO, LCMO-2.5%NiO, and LCMO-5%CuO, whereas a second-order phase transition was observed in LCMO-5%NiO, LCMO-2.5%CuO, LCMO-2.5%CoO, and LCMO-5%CoO. The change of order of magnetic phase transition was attributed to the Mn-O-Mn interaction with the diffusion of M ions into the LCMO matrix and particle size reduction [58], as explained earlier.

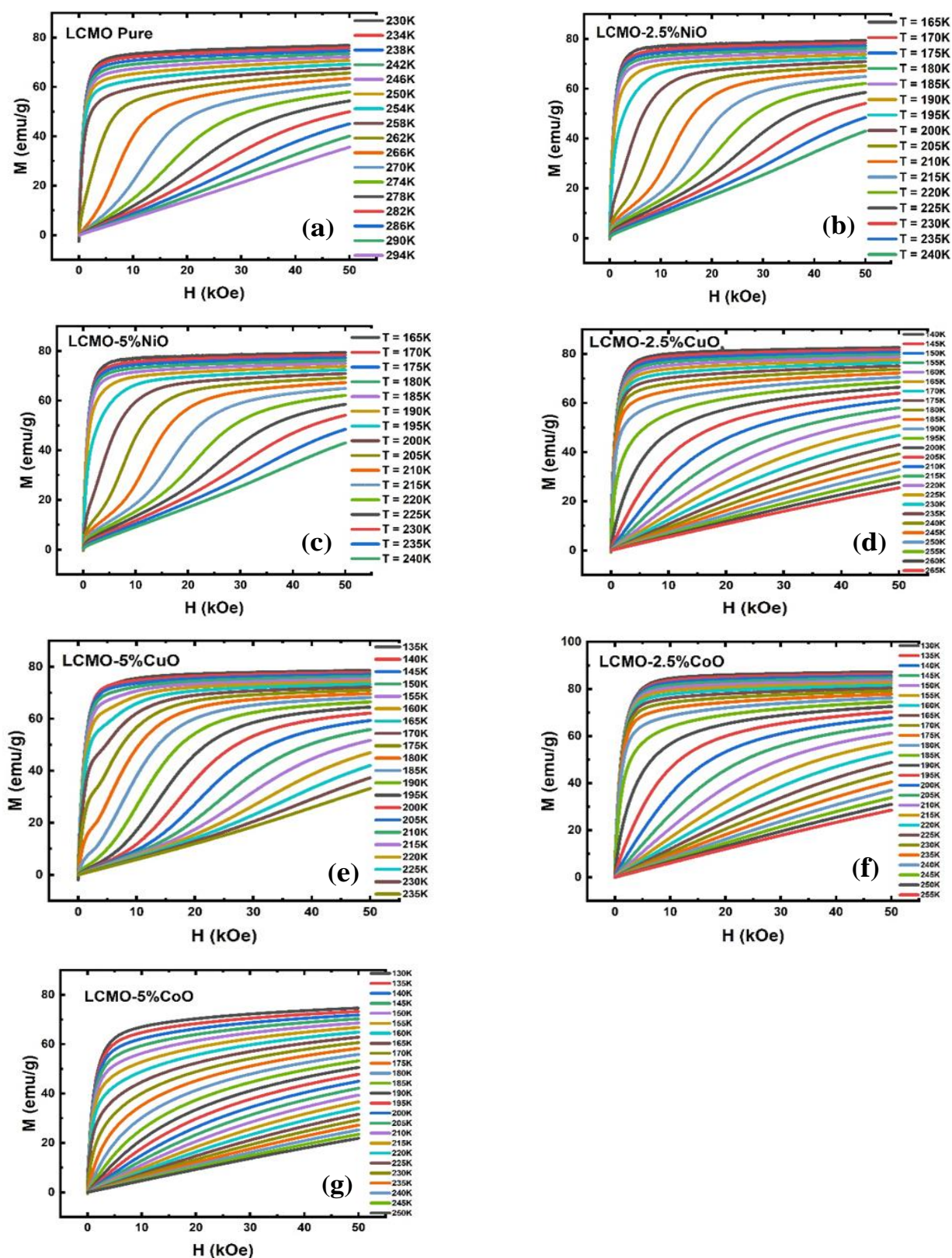


Figure 5. Isothermal magnetization curves for LCMO–MO composite samples (a) LCMO-pure, (b) LCMO-2.5% NiO, (c) LCMO-5% NiO, (d) LCMO-2.5% CuO, (e) LCMO-5% CuO, and (f) LCMO-2.5%CoO, (g) LCMO-5%CoO.

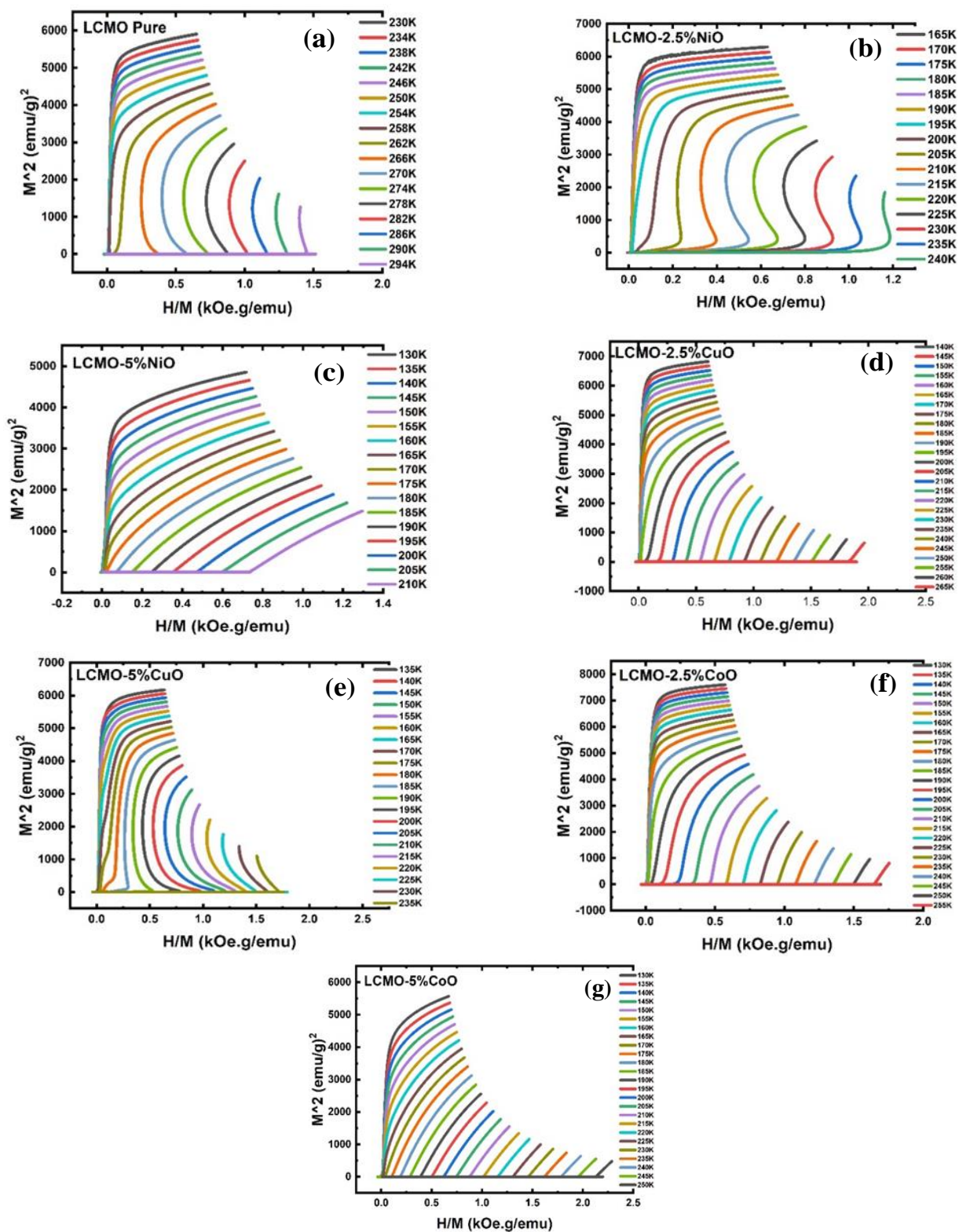


Figure 6. Arrott plots for LCMO–MO composite samples (a) LCMO-pure, (b) LMCO-2.5% NiO, (c) LMCO-5% NiO, (d) LCMO-2.5% CuO, (e) LCMO-5% CuO, and (f) LCMO-2.5%CoO, (g) LCMO-5%CoO.

From M vs. H curves in Figure 5 at different temperatures, the change in magnetic entropy of the sample was evaluated. The difference in magnetization was proportional to the change in entropy. The magnetic entropy change (ΔS_M) was one of the parameters to

evaluate the material's magnetocaloric property. The isothermal magnetic entropy change was computed using the thermodynamic Maxwell relation [59]:

$$\Delta S_M = \mu_0 \int_{H_i}^{H_f} \left(\frac{\partial M}{\partial T} \right)_H dH \quad (3)$$

$$\Delta S_M = \frac{\mu_0}{\Delta T} \left[\int_0^{H_f} M(T + \Delta T, H) dH - \int_0^{H_f} M(T, H) dH \right] \quad (4)$$

Numerically calculated as:

$$-\Delta S_M(H, T) = \sum \frac{M_i - M_{i+1}}{T_{i+1} - T_i} \Delta H_i \quad (5)$$

where H_i and H_f are the initial and final external applied fields and μ_0 is the permeability of free space. The $-\Delta S_M$ was calculated from the isothermal magnetization curve of Figure 5. This negative change in entropy with the temperature at different applied external field values (1–5 T) was plotted in Figure 7. The change in entropy was negative because heat was released when the magnetic field changed adiabatically. In other words, for an adiabatic process, a cooling effect during this phenomenon was observed. It was observed that this change in entropy reached a maximum at the phase transition temperature and increased with increase in the external field applied.

The maximum change in magnetic entropy (ΔS_M^{max}) and the FWHM of the plots were evaluated from the entropy change graph, Figure 7, and presented in Tables 4–6 for LCMO–NiO, LCMO–CuO, and LCMO–CoO samples, respectively. It was evident that the ΔS_M increased with the increase in strength of the applied field. The magnetic entropy change was at a maximum at 5 T for all the samples, because the large applied magnetic field induced higher ferromagnetic ordering in the sample. First, the maximum magnetic entropy change obtained for pristine LCMO was $4.75 \text{ J Kg}^{-1} \text{ K}^{-1}$ at 1 T, significantly higher than the recorded value of $1.2 \text{ J Kg}^{-1} \text{ K}^{-1}$ at 1.5 T [51]. A consistent trend of decrease in the maximum magnetic entropy and peak broadening with the increase in the metal oxide content was observed in all samples. The broadening of the peak was further verified by the increase in FWHM of the plot as the content of respective metal oxide increased. The most significant magnetic entropy drop from the pure LCMO was seen in LCMO–5%NiO. The change in magnetic entropy dropped from $8.77 \text{ J Kg}^{-1} \text{ K}^{-1}$ in pure LCMO to $3.24 \text{ J Kg}^{-1} \text{ K}^{-1}$ in LCMO–5%NiO at 5T. The plot's most significant increase in FWHM was for the LCMO–5%CoO sample. The FWHM increased from 24.63 K in pure LCMO to 64.09 K in LCMO–5%CoO. This defined the operational temperature for the samples, which increased significantly for LCMO–5%CoO. This increase in FWHM was observed in smaller amounts in other samples but was still significant, improving the practical application. The decrease in ΔS_M^{max} value was primarily attributed to the antiferromagnetic insulation of the LCMO by metal oxides [25]. The ΔS_M^{max} values were independent on temperature, except for LCMO–5%CuO, where ΔS_M^{max} shifted to higher temperature with the increased field. The magnetic inhomogeneity played a significant role in both ΔS_M^{max} reduction and increase in the FWHM values of the composite. The volume fraction of the LCMO decreased with increased metal oxide content. This also reduced the fraction of ferromagnetic spins compared to the pure sample [60].

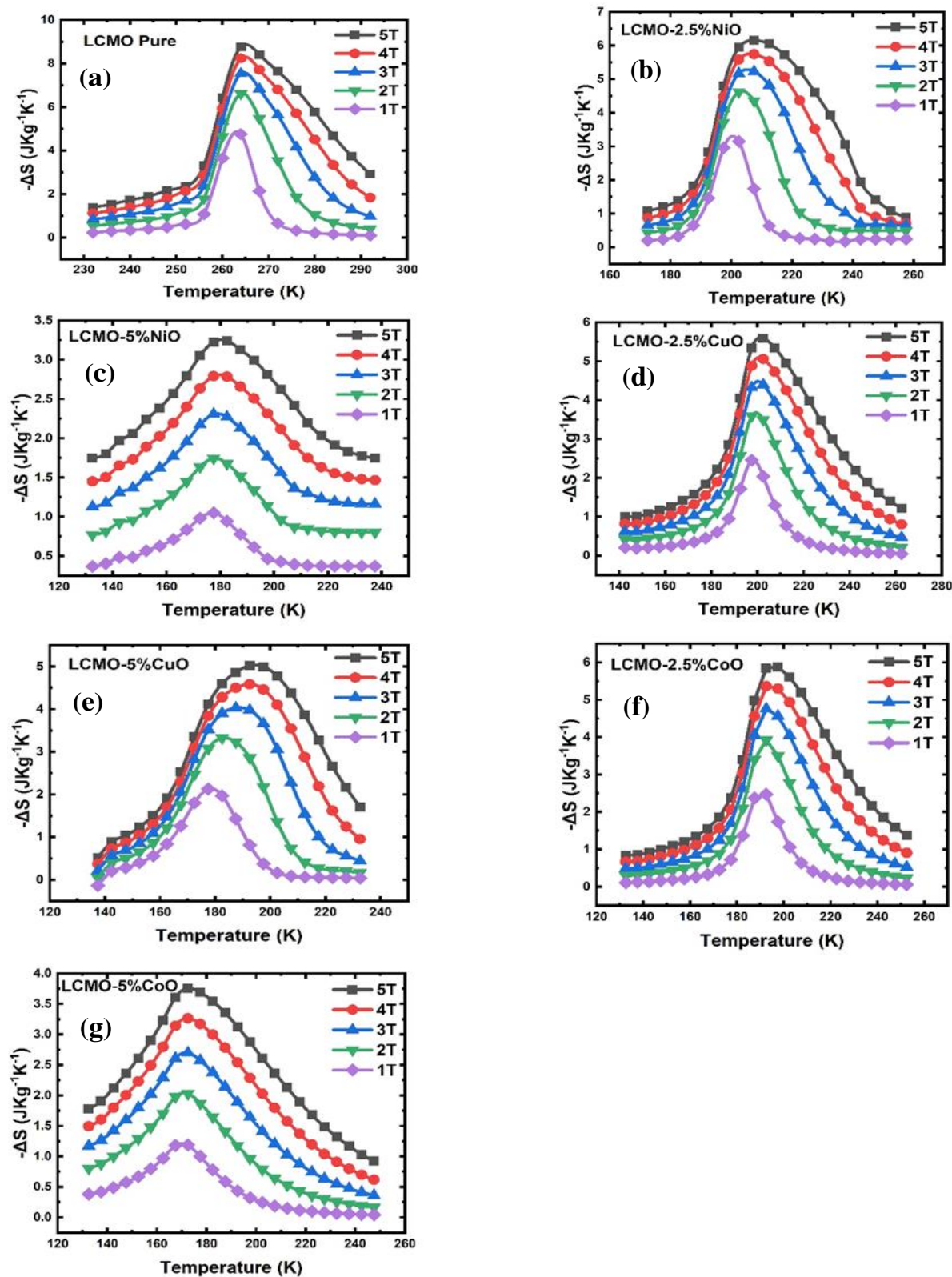


Figure 7. Temperature and magnetic field dependence of magnetic entropy change for LCMO–MO composite samples (a) LCMO-pure, (b) LMCO-2.5% NiO, (c) LMCO-5% NiO, (d) LCMO-2.5% CuO, (e) LCMO-5% CuO, and (f) LCMO-2.5%CoO, (g) LCMO-5%CoO.

Table 4. Magnetic field dependence of maximum entropy change, and FWHM of LCMO–NiO composite samples.

Field(T)	LCMO		LCMO–2.5%NiO		LCMO–5%NiO	
	ΔS_{max} (J·Kg ⁻¹ K ⁻¹)	FWHM (K)	ΔS_{max} (J·Kg ⁻¹ K ⁻¹)	FWHM (K)	ΔS_{max} (J·Kg ⁻¹ K ⁻¹)	FWHM (K)
1.0	4.75	8.86	3.14	14.14	1.05	29.12
2.0	6.61	13.31	4.62	20.38	1.74	33.68
3.0	7.54	17.36	5.22	27.18	2.30	38.50
4.0	8.23	21.14	5.74	33.93	2.79	43.12
5.0	8.77	24.63	6.16	39.45	3.24	47.10

Table 5. Magnetic field dependence of maximum entropy change, and FWHM of LCMO–CuO composite samples.

Field(T)	LCMO		LCMO–2.5%CuO		LCMO–5%CuO	
	ΔS_{max} (J·Kg ⁻¹ K ⁻¹)	FWHM (K)	ΔS_{max} (J·Kg ⁻¹ K ⁻¹)	FWHM (K)	ΔS_{max} (J·Kg ⁻¹ K ⁻¹)	FWHM (K)
1.0	4.75	8.86	2.45	19.79	2.12	25.75
2.0	6.61	13.31	3.59	26.73	3.32	32.47
3.0	7.54	17.36	4.39	32.30	4.02	39.11
4.0	8.23	21.14	5.05	37.12	4.58	46.05
5.0	8.77	24.63	5.59	41.72	5.02	53.14

Table 6. Magnetic field dependence of maximum entropy change, and FWHM of LCMO–CoO composite samples.

Field(T)	LCMO		LCMO–2.5%CoO		LCMO–5%CoO	
	ΔS_{max} (J·Kg ⁻¹ K ⁻¹)	FWHM (K)	ΔS_{max} (J·Kg ⁻¹ K ⁻¹)	FWHM (K)	ΔS_{max} (J·Kg ⁻¹ K ⁻¹)	FWHM (K)
1.0	4.75	8.86	2.47	19.70	1.18	42.18
2.0	6.61	13.31	3.92	26.45	2.02	52.30
3.0	7.54	17.36	4.75	32.20	2.69	58.04
4.0	8.23	21.14	5.36	37.49	3.26	61.72
5.0	8.77	24.63	5.87	42.85	3.75	64.09

Other than this, unintentional minor doping of metal ions on the B-site of the LCMO perovskite replacing the Mn ions could also reduce ΔS_M^{max} [57,58]. The published literature shows that the Mn ions in the Ca²⁺ substituted LaMnO₃ exhibit double-exchange interaction. Mn ions exist in two different oxidation states, +3 and +4, due to the presence of La³⁺ and Ca²⁺ cations in the A-site [61–66]. The magnetic Mn³⁺ and Mn⁴⁺ cations bonded through non-magnetic oxygen anion induce the hopping of electrons between the cations through oxygen to attain the least energy state. This is called double-exchange interaction. This phenomenon promotes ferromagnetic ordering. The replacement of such transition metal ions with M cations could minimize this delocalization of electrons and decrease the ferromagnetic ordering. Eventually, yielding a lower change in magnetic entropy [52].

The magnetic entropy change ΔS_M is proportional to the strength of the magnetic field. The ΔS_M value may be affected in the composite nanoparticles due to individual elements' properties. The effect of minority phases and demagnetization fields on the ΔS_M value in the composite can be studied by fitting the numerical formula at a fixed temperature:

$$\Delta S(H) = CH^N \quad (6)$$

where C is a constant, and N is the exponent obtained from experimental fitting that determines the sensitivity of magnetic entropy change to the applied field. The higher value

of N signifies higher sensitivity of the entropy change to the applied field. The exponent N was derived by fitting the experimental data at respective temperatures. Figure 8 shows the change in exponent N at different temperatures. From Figure 8, it is seen that the exponent N was at a minimum at T_C and exhibited a minor increase at temperatures below T_C and a significant increase at temperatures above T_C , which was expected [17]. Below T_C , the material was in the ferromagnetic phase, so the magnetic entropy did not change significantly due to the externally applied field. In contrast, above T_C , the paramagnetic phase of the material was highly influenced by the externally applied field, which substantially increased the N value.

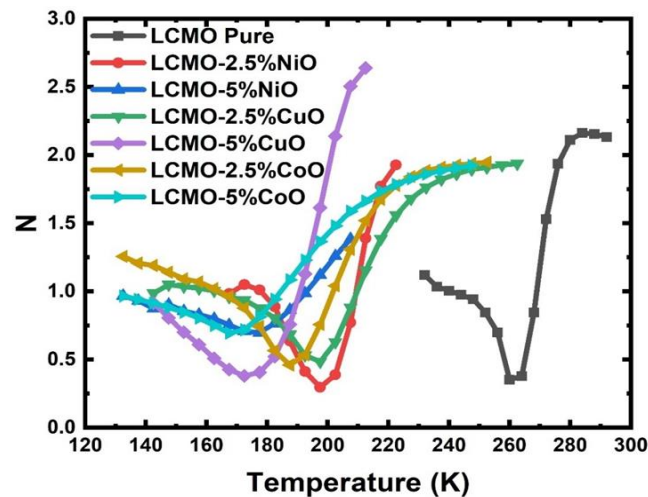


Figure 8. Exponent order N of LCMO–MO composite samples.

One of the most important parameters to quantify the magnetocaloric property of a material is RCP. It quantifies the heat energy transferred in a complete ideal magnetic refrigeration cycle. This accounts for the maximum change in entropy and the operational temperature of the given material, as given mathematically by the equations:

$$RCP = |-\Delta S_M^{max}| \times \delta T_{FWHM} \quad (7)$$

where ΔS_M^{max} is the maximum value of entropy changes at the given applied field (peak of ΔS_M vs. T plot), and δT_{FWHM} is the FWHM of the ΔS_M vs. T plot.

RCP was calculated using the data from Tables 4–6 and listed in Table 7 for all the samples. Figure 9 displays the RCPs at different applied magnetic fields from 1–5 T. We observed that the RCP values increased with the applied magnetic field. This was because the increase in change in entropy with the increasing magnetic field improved ferromagnetic ordering, and RCP was linearly related to the change in entropy, as given by the formula. The RCP of all composite samples increased, compared with the pristine LCMO except for LCMO–5%NiO. The highest RCP value of 266.89 JKg^{-1} was recorded for LCMO–5%CuO samples, which was 23.4% higher than the 213.13 JKg^{-1} observed for the pure LCMO at the 5T applied field. This was a substantial gain, considering the decrease in ΔS_{max} values, which was again attributed to the magnetic inhomogeneity introduced by the antiferromagnetic nature of the metal oxides [45,47]. The loss in magnetic entropy change was compensated for more than enough by broadening the peak, which increased the RCP. The decrease in RCP for LCMO–5%NiO was because of the small increment in the FWHM of the curve. This could be credited to the difference in phase transition temperature of the metal oxides with respect to LCMO [49]. The phase transition temperature for NiO was 525 K which was farther away from 258 K for LCMO compared to 230 K for CuO and 291 K for CoO. Due to this high difference in magnetic phase transition temperature, the RCP for a higher content of NiO in LCMO dropped to 152.71 JKg^{-1} . From this observation, it emerged

that the addition of MO as a secondary phase in LCMO samples indeed enhanced their cooling efficiency. The field dependence of RCP could also be studied using the relation:

$$RCP(H) = DH^R \quad (8)$$

where C is a constant and R is the exponent obtained from experimental fitting that determines the sensitivity of RCP to the externally applied field. The obtained R -value is shown in Table 8. A small drop in R -value with composite formation for all samples, except $\text{La}_{0.7}\text{Ca}_{0.3}\text{MnO}_3\text{-}2.5\%\text{NiO}$, was observed. This drop in R -value was reasonably close to 1 for all samples, which signified that RCP had an almost linear dependence on the externally applied field.

Table 7. Field dependent RCP values for LCMO-MO composite samples.

Sample	RCP ($\text{J}\cdot\text{Kg}^{-1}$)				
	1 T	2 T	3 T	4 T	5 T
LCMO	42.15	88.07	130.93	174.21	216.12
LCMO-2.5%NiO	44.51	94.19	142.17	194.92	243.05
LCMO-5%NiO	30.58	58.75	88.83	120.41	152.71
LCMO-2.5%CuO	48.62	96.15	142.02	187.77	233.37
LCMO-5%CuO	54.85	107.97	157.51	211.12	266.89
LCMO-2.5%CoO	48.79	103.76	153.25	201.16	251.78
LCMO-5%CoO	50.04	106.15	156.66	201.52	240.88

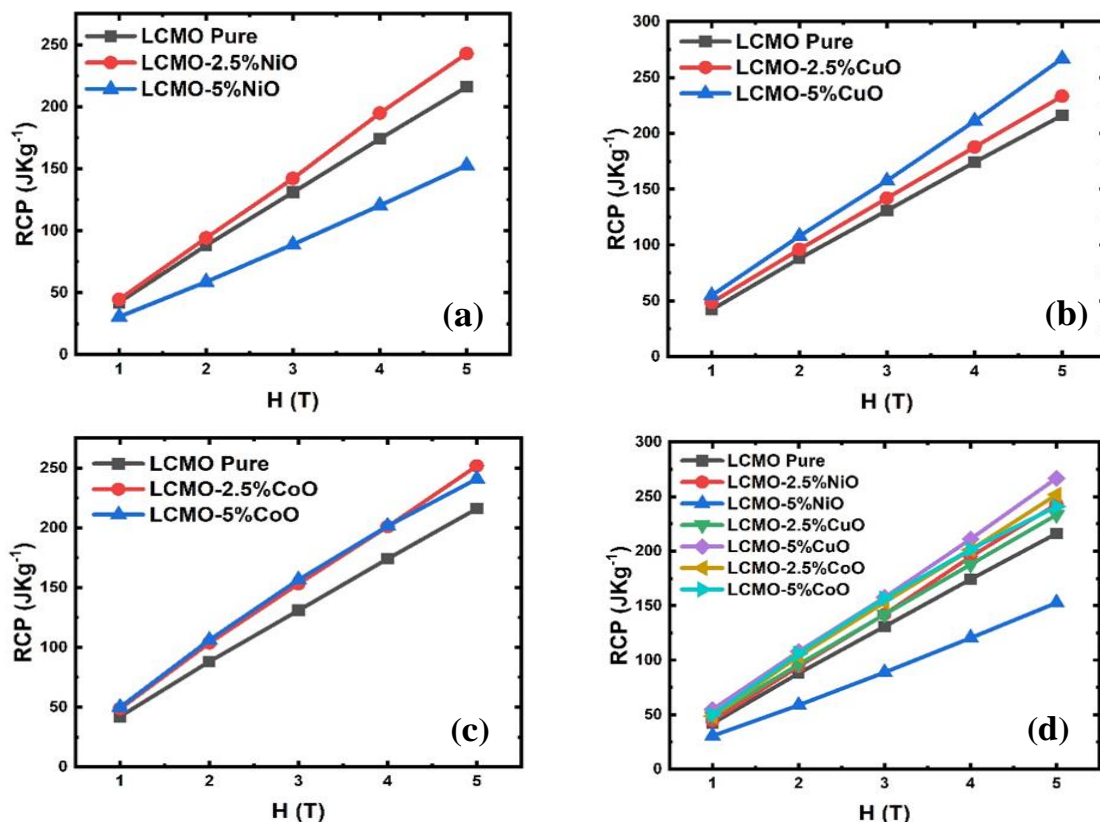


Figure 9. RCP of LACMO-MO composite samples (a) LMCO- $x\%$ NiO, (b) LCMO- $x\%$ CuO, (c) LCMO- $x\%$ CoO, and (d) LCMO- $x\%$ MO.

Table 8. R-value for LCMO-MO composite samples.

Sample	R-Value
LCMO	1.01
LCMO-2.5%NiO	1.05
LCMO-5%NiO	0.99
LCMO-2.5%CuO	0.97
LCMO-5%CuO	0.97
LCMO-2.5%CoO	1.01
LCMO-5%CoO	0.98

6. Conclusions

In summary, the study highlights the influence of the metal-oxide second phase on the magnetocaloric effect of LCMO–MO composite samples. The XRD revealed that MO did not enter into the LCMO matrix. The temperature dependence of the magnetization shows that the T_C decreases in the case of composite samples, as compared to LCMO samples. This decrease in T_C is due to incorporating the antiferromagnetic second MO phase in the pure LCMO samples. The magnetic entropy changes of all the samples showed a maximum around their respective T_C values, and its magnitude decreased in composite samples compared to pristine LCMO. However, the operating temperature range and RCP of the composite samples increased. The highest RCP value of 266.89 J Kg^{-1} was observed in LCMO–5%CuO samples, which was 23.4% higher than the 213.13 J Kg^{-1} observed for the pure LCMO at an externally applied field of 5T. The enhanced RCP of these composites make them attractive for potential applications.

Author Contributions: Conceptualization, S.R.M.; Methodology, S.D, J.C. and D.N.; Validation, A.K.P.; Formal Analysis, S.D., S.K. and A.K.P.; Investigation, S.R.M.; Resources, S.R.M.; Data Curation, S.D. and S.K.; Writing—original Draft Preparation, S.D., S.K. and S.R.M.; Writing—Review & Editing, S.K. and S.R.M.; Visualization, S.R.M.; Supervision, S.R.M. and S.K.; Project Administration, S.R.M.; Funding Acquisition, S.R.M. and A.K.P. All authors have read and agreed to the published version of the manuscript.

Funding: The magnetic measurements were performed at the State University of New York (SUNY), Buffalo State, and supported by the National Science Foundation Award No. DMR-2213412 and Office of Undergraduate Research, Buffalo State. Mishra acknowledges FRG funds from the University of Memphis, Memphis, TN, USA.

Institutional Review Board Statement: Not applicable.

Informed Consent Statement: Not applicable.

Data Availability Statement: The data presented in this study are openly available on request.

Conflicts of Interest: The authors declare no conflict of interest.

References

- Wang, Y.; Zhang, H.; Liu, E.; Zhong, X.; Tao, K.; Wu, M.; Xing, C.; Xiao, Y.; Liu, J.; Long, Y. Outstanding Comprehensive Performance of $\text{La}(\text{Fe}, \text{Si})_{13} \text{H}_y/\text{In}$ Composite with Durable Service Life for Magnetic Refrigeration. *Adv. Electron. Mater.* **2018**, *4*, 1700636. [[CrossRef](#)]
- Li, L.; Yan, M. Recent progresses in exploring the rare earth based intermetallic compounds for cryogenic magnetic refrigeration. *J. Alloys Compd.* **2020**, *823*, 153810. [[CrossRef](#)]
- Gottschall, T.; Skokov, K.P.; Fries, M.; Taubel, A.; Radulov, I.; Scheibel, F.; Benke, D.; Riegg, S.; Gutfleisch, O. Making a Cool Choice: The Materials Library of Magnetic Refrigeration. *Adv. Energy Mater.* **2019**, *9*, 1901322. [[CrossRef](#)]
- Gschneidner, K.A., Jr.; Pecharsky, V.; Pecharsky, A.; Zimm, C. Recent Developments in Magnetic Refrigeration. *Mater. Sci. Forum* **1999**, *315–317*, 69–76. [[CrossRef](#)]
- Kitanovski, A. Energy Applications of Magnetocaloric Materials. *Adv. Energy Mater.* **2020**, *10*, 1903741. [[CrossRef](#)]
- Weiss, P.; Piccard, A. The magnetocaloric phenomenon. *J. Phys. Appl.* **1917**, *7*, 103–109. [[CrossRef](#)]
- Gschneidner, K.A., Jr.; Pecharsky, V. Magnetic refrigeration materials. *J. Appl. Phys.* **1999**, *85*, 5365–5368. [[CrossRef](#)]
- Moya, X.; Kar-Narayan, S.; Mathur, N.D. Caloric materials near ferroic phase transitions. *Nat. Mater.* **2014**, *13*, 439–450. [[CrossRef](#)]

9. Lyubina, J.; Schäfer, R.; Martin, N.; Schultz, L.; Gutfleisch, O. Novel Design of La(Fe,Si)₁₃ Alloys Towards High Magnetic Refrigeration Performance. *Adv. Mater.* **2010**, *22*, 3735–3739. [[CrossRef](#)]
10. Provenzano, V.; Shapiro, A.J.; Shull, R.D. Reduction of hysteresis losses in the magnetic refrigerant Gd₅Ge₂Si₂ by the addition of iron. *Nature* **2004**, *429*, 853–857. [[CrossRef](#)]
11. Lyubina, J.; Hannemann, U.; Cohen, L.F.; Ryan, M.P. Novel La(Fe,Si)₁₃/Cu Composites for Magnetic Cooling. *Adv. Energy Mater.* **2012**, *2*, 1323–1327. [[CrossRef](#)]
12. Bejar, M.; Sdiri, N.; Hussein, M.; Mazen, S.; Dhahri, E. Magnetocaloric effect on strontium vacancies in polycrystalline La_{0.7}Sr_{0.3-x}□_xMnO₃. *J. Magn. Magn. Mater.* **2007**, *316*, e566–e568. [[CrossRef](#)]
13. Kallel, N.; Kallel, S.; Hagaza, A.; Oumezzine, M. Magnetocaloric properties in the Cr-doped La_{0.7}Sr_{0.3}MnO₃ manganites. *Phys. B Condens. Matter* **2009**, *404*, 285–288. [[CrossRef](#)]
14. Ehsani, M.H.; Kameli, P.; Ghazi, M.E.; Razavi, F.S.; Taheri, M. Tunable magnetic and magnetocaloric properties of La_{0.6}Sr_{0.4}MnO₃ nanoparticles. *J. Appl. Phys.* **2013**, *114*, 223907. [[CrossRef](#)]
15. Chau, N.; Niem, P.Q.; Nhat, H.N.; Luong, N.H.; Tho, N.D. Influence of Cu substitution for Mn on the structure, magnetic, magnetocaloric and magnetoresistance properties of La_{0.7}Sr_{0.3}MnO₃ perovskites. *Phys. B Condens. Matter* **2003**, *327*, 214–217. [[CrossRef](#)]
16. Hamad, M.; Hemedat, O.; Alamri, H.R.; Mohamed, A.; Harb, M.E. Strong tailoring magnetocaloric effect in highly (001)-oriented La_{0.7}Sr_{0.3}MnO₃ thin films. *J. Mater. Res. Technol.* **2021**, *11*, 1356–1361. [[CrossRef](#)]
17. Pękała, M.; Pękała, K.; Drozd, V.; Staszkiwicz, K.; Fagnard, J.-F.; Vanderbemden, P. Magnetocaloric and transport study of poly- and nanocrystalline composite manganites La_{0.7}Ca_{0.3}MnO₃/La_{0.8}Sr_{0.2}MnO₃. *J. Appl. Phys.* **2012**, *112*, 023906. [[CrossRef](#)]
18. M’Nassri, R. Searching the conditions for a table-like shape of the magnetic entropy in the magnetocaloric LBMO_{2.98}/LBMO_{2.95} composite. *Eur. Phys. J. Plus* **2016**, *131*, 392. [[CrossRef](#)]
19. Mbarek, H.; M’Nasri, R.; Cheikhrouhou-Koubaa, W.; Cheikhrouhou, A. Magnetocaloric effect near room temperature in (1-y)La_{0.8}Ca_{0.05}K_{0.15}MnO₃/y La_{0.8}K_{0.2}MnO₃ composites. *Phys. Status Solidi A* **2014**, *211*, 975–979. [[CrossRef](#)]
20. Jerbi, A.; Krichene, A.; Chniba-Boudjada, N.; Boujelben, W. Magnetic and magnetocaloric study of manganite compounds Pr_{0.5}A_{0.05}Sr_{0.45}MnO₃ (A=Na and K) and composite. *Phys. B Condens. Matter* **2015**, *477*, 75–82. [[CrossRef](#)]
21. Ezaami, A.; Chaaba, I.; Cheikhrouhou-Koubaa, W.; Cheikhrouhou, A.; Hlil, E. Enhancement of magnetocaloric properties around room temperature in (1-x)La_{0.7}Ca_{0.25}Sr_{0.05}MnO₃/xLa_{0.7}Ca_{0.2}Sr_{0.1}MnO₃ system (0 ≤ x ≤ 1). *J. Alloys Compd.* **2018**, *735*, 2331–2335. [[CrossRef](#)]
22. Akça, G.; Çetin, S.K.; Ekicibil, A. Composite xLa_{0.7}Ca_{0.2}Sr_{0.1}MnO₃/(1-x)La_{0.7}Te_{0.3}MnO₃ materials: Magnetocaloric properties around room temperature. *J. Mater. Sci. Mater. Electron.* **2020**, *31*, 6796–6808. [[CrossRef](#)]
23. Gschneidner, K.A., Jr.; Pecharsky, V.K. Magnetocaloric Materials. *Annu. Rev. Mater. Sci.* **2000**, *30*, 387–429. [[CrossRef](#)]
24. El Boukili, A.; Mounkachi, O.; Hamedoun, M.; Lachkar, P.; Hlil, E.; Benyoussef, A.; Balli, M.; Ez-Zahraouy, H. A study of structural, magnetic and magnetocaloric properties of (1-x)La_{0.6}Ca_{0.4}MnO₃/xMn₂O₃ composite materials. *J. Alloys Compd.* **2020**, *859*, 158392. [[CrossRef](#)]
25. Anwar, M.; Ahmed, F.; Danish, R.; Koo, B.H. Impact of Co₃O₄ phase on the magnetocaloric effect and magnetoresistance in La_{0.7}Sr_{0.3}MnO₃/Co₃O₄ and La_{0.7}Ca_{0.3}MnO₃/Co₃O₄ ceramic composites. *Ceram. Int.* **2015**, *41*, 631–637. [[CrossRef](#)]
26. Nasri, M.; Khelifi, J.; Laifi, J.; Hcini, F.; Alzahrani, B.; Bouazizi, M.L.; Dhahri, E.; Hlil, E. Structural, magnetic and theoretical investigation of the magnetocaloric effect of La_{0.6}Sr_{0.4}MnO₃/x(Sb₂O₃) compound. *Phase Transit.* **2021**, *94*, 170–182. [[CrossRef](#)]
27. Gavrilova, T.; Gilmudtinov, I.; Deeva, J.; Chupakhina, T.; Lyadov, N.; Faizrakhmanov, I.; Milovich, F.; Kabirov, Y.; Eremina, R. Magnetic and magnetocaloric properties of (1-x)La_{0.7}Sr_{0.3}MnO₃/xNaF composites. *J. Magn. Magn. Mater.* **2018**, *467*, 49–57. [[CrossRef](#)]
28. Neupane, D.; Hulsebosch, L.; Pathak, A.K.; Mishra, S.R. Magnetocaloric Study of La_{0.45}Nd_{0.25}Sr_{0.3}MnO₃/MO (MO=CuO, CoO, and NiO) Nanocomposites. *IEEE Trans. Magn.* **2021**, *58*, 1–8. [[CrossRef](#)]
29. Wang, F.; Fu, W.; Jiang, C.; Li, J.; Huang, J. Exchange Bias Effect in LaFeO₃: La_{0.7}Ca_{0.3}MnO₃ Composite Thin Films. *Coatings* **2021**, *11*, 1125. [[CrossRef](#)]
30. Lau, L.; Lim, K.; Chok, S.; Ishak, A.; Hon, X.; Wong, Y.; Kechik, M.A.; Chen, S.; Ibrahim, N.; Miryala, M.; et al. Effect of NiO Nanoparticle Addition on the Structural, Microstructural, Magnetic, Electrical, and Magneto-Transport Properties of La_{0.67}Ca_{0.33}MnO₃ Nanocomposites. *Coatings* **2021**, *11*, 835. [[CrossRef](#)]
31. Phong, P.; Khiem, N.; Dai, N.; Manh, D.; Hong, L.; Phuc, N. Influence of Al₂O₃ on low-field spin-polarized tunneling magnetoresistance of (1-x)La_{0.7}Ca_{0.3}MnO₃+x Al₂O₃ composites. *Mater. Lett.* **2009**, *63*, 353–356. [[CrossRef](#)]
32. Hwang, H.Y.; Cheong, S.-W.; Ong, N.P.; Batlogg, B. Spin-Polarized Intergrain Tunneling in La₂/3Sr₁/3MnO₃. *Phys. Rev. Lett.* **1996**, *77*, 2041–2044. [[CrossRef](#)] [[PubMed](#)]
33. Tadić, M.; Panjan, M.; Marković, D. NiO/SiO₂ nanostructure and the magnetic moment of NiO nanoparticles. *Mater. Lett.* **2010**, *64*, 2129–2131. [[CrossRef](#)]
34. Varma, A.; Mukasyan, A.S.; Rogachev, A.S.; Manukyan, K.V. Solution Combustion Synthesis of Nanoscale Materials. *Chem. Rev.* **2016**, *116*, 14493–14586. [[CrossRef](#)] [[PubMed](#)]
35. Kapanja, L.; Milosevic, I.; Panjan, M.; Damjanovic, V.; Tadic, M. Sol-gel combustion synthesis, particle shape analysis and magnetic properties of hematite (α-Fe₂O₃) nanoparticles embedded in an amorphous silica matrix. *Appl. Surf. Sci.* **2016**, *362*, 380–386. [[CrossRef](#)]

36. Patil, J.; Nadargi, D.; Gurav, J.; Mulla, I.; Suryavanshi, S. Synthesis of glycine combusted NiFe₂O₄ spinel ferrite: A highly versatile gas sensor. *Mater. Lett.* **2014**, *124*, 144–147. [[CrossRef](#)]
37. Yang, J.; Guo, Q.; Wen, X.; Gao, X.; Peng, Q.; Li, Q.; Ma, D.; Li, Z. Pyrene-based blue AIEgens: Tunable intramolecular conjugation, good hole mobility and reversible mechanochromism. *J. Mater. Chem. C* **2016**, *4*, 8506–8513. [[CrossRef](#)]
38. Azadmanjiri, J.; Ebrahimi, S.A.S. Influence of stoichiometry and calcination condition on the microstructure and phase constitution of NiFe₂O₄ powders prepared by sol-gel autocombustion method. *Phys. Status Solidi C* **2004**, *1*, 3414–3417. [[CrossRef](#)]
39. Bahadur, D.; Fischer, W.; Rane, M. In-situ high-temperature X-ray diffraction studies of non-stoichiometric Ni–Zr substituted barium hexagonal ferrites prepared by citrate precursor route. *Mater. Sci. Eng. A* **1998**, *252*, 109–116. [[CrossRef](#)]
40. Anwar, M.S.; Ahmed, F.; Kim, G.W.; Heo, S.N.; Koo, B.H. The interplay of Ca and Sr in the bulk magnetocaloric La_{0.7}Sr_(0.3–x)Ca_xMnO₃ (x = 0, 0.1 and 0.3) manganite. *J. Korean Phys. Soc.* **2013**, *62*, 1974–1978. [[CrossRef](#)]
41. Ayuela, A.; Klein, D.J.; March, N.H. Neel temperature of antiferromagnets for phase transitions driven by spin-wave interactions. *Croat. Chem. Acta* **2013**, *86*, 463–467. [[CrossRef](#)]
42. Kimura, T.; Sekio, Y.; Nakamura, H.; Siegrist, T.; Ramirez, A.P. Cupric oxide as an induced-multiferroic with high-TC. *Nat. Mater.* **2008**, *7*, 291–294. [[CrossRef](#)]
43. El Maalam, K.; Balli, M.; Habouti, S.; Dietze, M.; Hamedoun, M.; Hlil, E.K.; Es-Souni, M.; El Kenz, A.; Benyoussef, A.; Mounkachi, O. Composite (La_{0.45}Nd_{0.25})Sr_{0.3}MnO₃/5CuO materials for magnetic refrigeration applications. *J. Magn. Magn. Mater.* **2018**, *449*, 25–32. [[CrossRef](#)]
44. Patterson, A.L. The Scherrer Formula for X-Ray Particle Size Determination. *Phys. Rev. Series I* **1939**, *56*, 978–982. [[CrossRef](#)]
45. Shankar, K.; Kar, S.; Subbanna, G.; Raychaudhuri, A. Enhanced ferromagnetic transition temperature in nanocrystalline lanthanum calcium manganese oxide (La_{0.67}Ca_{0.33}MnO₃). *Solid State Commun.* **2004**, *129*, 479–483. [[CrossRef](#)]
46. Cureton, W.F.; Palomares, R.I.; Walters, J.; Tracy, C.L.; Chen, C.-H.; Ewing, R.C.; Baldinozzi, G.; Lian, J.; Trautmann, C.; Lang, M. Grain size effects on irradiated CeO₂, ThO₂, and UO₂. *Acta Mater.* **2018**, *160*, 47–56. [[CrossRef](#)]
47. Dipesh, D.N.; Wang, L.; Adhikari, H.; Alam, J.; Mishra, S. Influence of Al³⁺ doping on structural and magnetic properties of CoFe_{2–x}Al_xO₄ Ferrite nanoparticles. *J. Alloys Compd.* **2016**, *688*, 413–421. [[CrossRef](#)]
48. Zulueta, Y.A.; Dawson, J.A.; Mune, P.D.; Froeyen, M.; Nguyen, M.T. Oxygen vacancy generation in rare-earth-doped SrTiO₃. *Phys. Status Solidi B* **2016**, *253*, 2197–2203. [[CrossRef](#)]
49. Poudel, T.; Rai, B.; Yoon, S.; Guragain, D.; Neupane, D.; Mishra, S. The effect of gadolinium substitution in inverse spinel nickel ferrite: Structural, Magnetic, and Mössbauer study. *J. Alloys Compd.* **2019**, *802*, 609–619. [[CrossRef](#)]
50. Zhou, X.; Zhou, Y.; Zhou, L.; Wei, J.; Wu, J.; Yao, D. Effect of Gd and La doping on the structure, optical and magnetic properties of NiZnCo ferrites. *Ceram. Int.* **2018**, *45*, 6236–6242. [[CrossRef](#)]
51. Yang, H.; Zhu, Y.; Xian, T.; Jiang, J. Synthesis and magnetocaloric properties of La_{0.7}Ca_{0.3}MnO₃ nanoparticles with different sizes. *J. Alloys Compd.* **2013**, *555*, 150–155. [[CrossRef](#)]
52. Liu, M.F.; Du, Z.Z.; Xie, Y.L.; Li, X.; Yan, Z.B.; Liu, J.M. Unusual ferromagnetism enhancement in ferromagnetically optimal manganite La_{0.72y}Ca_{0.31y}Mn_{12y}RuyO₃ (0#y,0.3): The role of Mn–Ru t_{2g} super-exchange. *Sci. Rep.* **2015**, *5*, 9922. [[CrossRef](#)] [[PubMed](#)]
53. Beyreuther, E.; Grafström, S.; Eng, L.M.; Thiele, C.; Dörr, K. XPS investigation of Mn valence in lanthanum manganite thin films under variation of oxygen content. *Phys. Rev. B* **2006**, *73*, 155425. [[CrossRef](#)]
54. Gao, T.; Cao, S.; Liu, Y.; Zhang, Y.; Zhang, J. Cu-doping induced ferromagnetic insulating behavior and domain wall pinning effects in LaMnO₃. *Rare Met.* **2011**, *30*, 359–367. [[CrossRef](#)]
55. Goodenough, J.B.; Wold, A.; Arnott, R.J.; Menyuk, N. Relationship Between Crystal Symmetry and Magnetic Properties of Ionic Compounds Containing Mn³⁺. *Phys. Rev. Series I* **1961**, *124*, 373–384. [[CrossRef](#)]
56. He, X.; Zhong, W.; Au, C.T.; Du, Y. Size dependence of the magnetic properties of Ni nanoparticles prepared by thermal decomposition method. *Nanoscale Res. Lett.* **2013**, *8*, 446. [[CrossRef](#)]
57. Banerjee, B.K. On a generalized approach to first and second order magnetic transitions. *Phys. Lett.* **1964**, *12*, 16–17. [[CrossRef](#)]
58. Tang, W.; Lu, W.; Luo, X.; Wang, B.; Zhu, X.; Song, W.; Yang, Z.; Sun, Y. Particle size effects on La_{0.7}Ca_{0.3}MnO₃: Size-induced changes of magnetic phase transition order and magnetocaloric study. *J. Magn. Magn. Mater.* **2010**, *322*, 2360–2368. [[CrossRef](#)]
59. Pecharsky, V.K.; Gschneidne, K.A., Jr. Magnetocaloric effect and magnetic refrigeration. *J. Magn. Magn. Mater.* **1999**, *200*, 44–56. [[CrossRef](#)]
60. Ahmed, A.; Mohamed, H.; Diab, A.; Omar, E.Y. Crossover effect of magnetotransport and magnetocaloric effect in (La_{0.7}Ba_{0.3}MnO₃)_{1–x}/(Al₂O₃)_x composites. *J. Magn. Magn. Mater.* **2019**, *489*, 165388. [[CrossRef](#)]
61. Phan, T.-L.; Thanh, P.; Yen, P.; Zhang, P.; Thanh, T.; Yu, S. Ferromagnetic short-range order and magnetocaloric effect in Fe-doped LaMnO₃. *Solid State Commun.* **2013**, *167*, 49–53. [[CrossRef](#)]
62. Hcini, S.; Boudard, M.; Zemni, S.; Oumezzine, M. Effect of Fe-doping on structural, magnetic and magnetocaloric properties of Nd_{0.67}Ba_{0.33}Mn_{1–x}FexO₃ manganites. *Ceram. Int.* **2014**, *40*, 16041–16050. [[CrossRef](#)]
63. Bi, Y.; He, W.; Yang, T.; Wu, W.; Wen, J.; Yu, X.; Chen, F. The Effects of La Doping on the Crystal Structure and Magnetic Properties of Ni₂In-Type MnCoGe_{1–x}La_x (x = 0, 0.01, 0.03) Alloys. *Materials* **2021**, *14*, 3998. [[CrossRef](#)] [[PubMed](#)]
64. Afify, M.S.; El Faham, M.M.; Eldemerdash, U.; El Roubay, W.M.; El-Dek, S. Room temperature ferromagnetism in Ag doped LaMnO₃ nanoparticles. *J. Alloys Compd.* **2021**, *861*, 158570. [[CrossRef](#)]

-
65. Biswas, B.; Taran, S.; Pal, S. Study of magnetic and magnetocaloric properties in monovalent doped $\text{Pr}_{0.75}\text{Li}_{0.25}\text{MnO}_3$. *AIP Conf. Proc.* **2021**, *2352*, 020016. [[CrossRef](#)]
 66. Rahman, M.M.; Jamal, A.; Khan, S.B.; Faisal, M. Fabrication of Highly Sensitive Ethanol Chemical Sensor Based on Sm-Doped Co_3O_4 Nanokernels by a Hydrothermal Method. *J. Phys. Chem. C* **2011**, *115*, 9503–9510. [[CrossRef](#)]